# Structural and ferroelectric phase evolution in $[KNbO_3]_{1-x}[BaNi_{1/2}Nb_{1/2}O_{3-\delta}]_x$ ($x = 0,0.1$)

Christopher J. Hawley,[1] Liyan Wu,[2] Geoffrey Xiao,[1] Ilya Grinberg,[3] Andrew M. Rappe,[2,4]
Peter K. Davies,[2] and Jonathan E. Spanier[1,5,*]

[1]*Department of Materials Science & Engineering, Drexel University, Philadelphia, Pennsylvania 19104, USA*
[2]*Department of Materials Science & Engineering, University of Pennsylvania, Philadelphia, Pennsylvania 19104, USA*
[3]*Department of Chemistry, Bar Ilan University, Ramat-Gan 5290002, Israel*
[4]*Department of Chemistry, University of Pennsylvania, Philadelphia, Pennsylvania 19104, USA*
[5]*Department of Physics, Drexel University, Philadelphia, Pennsylvania 19104, USA*

(Received 22 January 2017; revised manuscript received 1 August 2017; published 28 August 2017)

The phase transition evolution for $[KNbO_3]_{1-x}[BaNi_{1/2}Nb_{1/2}O_{3-\delta}]_x$ ($x = 0,0.1$) is determined via complementary dielectric permittivity and Raman-scattering measurements. Raman scattering by optical phonons over the range of 100–1000 $cm^{-1}$ for 83 K $< T <$ 873 K reveals six discernible zone-center optical phonon modes. Mode behaviors are observed through structural and ferroelectric phases in the solid solution $x = 0.1$ and compared with those for end member $x = 0$ and with the results of temperature-dependent dielectric permittivity. Rigorous peak fitting analyses of spectra collected from the solid solution and end member indicate structural and ferroelectric phase transition temperatures that are close to those for the $KNbO_3$ end member despite the inclusion of 5 atomic % of ferroelectrically inactive Ni cations. Density functional theory calculations were performed in the solid solution and end member using both cation displacement and Berry phase-based methods. Differences in the electronic and polar properties between the solid solution and the end member highlights local and nonlocal characteristics, which are discussed in relation to the experimental data.

DOI: 10.1103/PhysRevB.96.054117

## I. INTRODUCTION

Ferroelectrics have long been recognized as an interesting alternative to conventional semiconductor junctions for photo-excited carrier separation and photovoltaic solar energy conversion [1–18], exhibiting the bulk photovoltaic (PV) effect [19–22] and other ferroelectric polarization-induced or polarization-influenced carrier separation mechanisms, including those due to domain walls and Schottky barriers. The design and realization of visible wavelength-absorbing ferroelectric oxide perovskites poses special challenges for practical photovoltaic solar energy conversion due to the inherently large band gap ($\gtrsim$2.7 eV) associated typically with an O 2$p$ valence and a transition metal $d$ conduction band. Inclusion of other $B$-site cations (e.g., Pd, Pt, etc.), substitutionally, within $PbTiO_3$ [23] has been proposed as a strategy for band gap lowering [24–27]. Introduction of Ni onto $B$-site $KNbO_3$ in the solid solution $[KNbO_3]_{1-x}[BaNi_{1/2}Nb_{1/2}O_{3-\delta}]_x$ ($x = 0.1$) (KBNNO) was shown to result in significant decrease in band gap without loss of ferroelectric ordering [10], and relatively large shift currents in KBNNO (compared with $BiFeO_3$) have been predicted [28]. Recently, room-temperature Raman-scattering spectra in bulk ceramic KBNNO have been reported [29] for several different values of $x$.

Incorporation of ferroelectrically inactive cations can be accomplished without complete suppression of ferroelectricity. However, concomitant decreases in ferroelectric phase transition temperature, $T_c$, with inactive cation concentration can be expected in accordance with well-known systems, e.g., Zr in $PbTiO_3$ (PZT) [30], and Sr in $BaTiO_3$, forming the well-known incipient ferroelectric solid solution $Ba_{1-x}Sr_xTiO_3$ (BST) [31]. Raman-scattering spectroscopy is effective for probing the onset of a phase transition with local correlation lengths as short as several unit cells. The structural evolution and determination of $T_c$ in $KNbO_3$ and related $A$-site ($A$ = Na, Li, La) solid solutions $ANbO_3$ (KNNO and KLNO) has been reported via temperature-dependent dielectric, Raman scattering, and infrared spectroscopic analyses [32–40]. Other studies of $T_c$ evolution in doped $KNbO_3$ have also been reported [41–45]. Unlike systems that involve isovalent substitutions, such as PZT, BST, KNNO, $KTa_{1-x}Nb_xO_3$, and $K_{1-x}Li_xNbO_3$, the aliovalent substitution of $Ni^{2+}$ onto the $B$-site of $KNbO_3$ is accompanied by formation of a neighboring O vacancy, producing localized tensile strain near the cation-vacancy pair. Ferroelectric phase stability is a key consideration for potential optoelectronic applications including PV solar energy conversion, making it important to consider the extent to which the substitutional incorporation of Ni cations influences the structural and ferroelectric phase stability in the solid solution KBNNO.

As summarized in Tables I and II, end member $KNbO_3$ possesses 15 modes, including 3 acoustic and 12 optical phonons. Of the optical phonons, by symmetry, three $A_1 + 4$ $E$ are first-order Raman active in the rhombohedral ($R3m$ or $C_{3v}^5$) phase with an $A_2$ phonon mode as Raman silent, four $A_1 + A_2 + 4$ $B_1 + 3$ $B_2$ in the orthorhombic ($Amm2$ or $C_{2v}^{14}$) phase, and three $A_1 + B_1 + 4$ $E$ in the tetragonal ($P4mm$ or $C_{4v}^1$) phase. First-order Raman scattering of the three $F_{1u} + F_{2u}$ modes is forbidden in the centrosymmetric cubic ($Pm3m$ or $O_h^1$) phase. Atomic site disorder lowers translational symmetry, effectively relaxing Raman selection rules. This increases phonon scattering rates, manifesting as broadened lineshapes, complicating determination of peak positions and mode assignments [42–44,46]. Nevertheless, Raman-active mode assignments and transition temperatures in solid solutions such as $(K,A)NbO_3$ have been made and can also be accomplished in $B$-site solid solution systems,

*jes53@drexel.edu

 

TABLE I. Twelve optical phonon modes of KNO, as predicted by Postnikov *et al.* [62] for the room temperature orthorhombic phase. Included are experimental values from this study.

| Mode | Symm. | Calculated Frequency ($cm^{-1}$) | Experimental Values ($cm^{-1}$) |
|---|---|---|---|
| | $B_2$ | soft | |
| $TO_1$ | $B_1$ | 232 | 250 |
| | $A_1$ | 257 | 296 |
| | $B_2$ | 185 | 192 |
| $TO_2$ | $B_1$ | 146 | [a] |
| | $A_1$ | 186 | 275 |
| | $B_2$ | 467 | 532 |
| $TO_3$ | $B_1$ | 528 | [b] |
| | $A_1$ | 593 | 596 |
| | $B_1$ | 297 | [c] |
| $TO_4$ | $A_1$ | 307 | [c] |
| | $A_2$ | 224 | [c] |

[a]indistinguishable with $B_2(TO_2)$
[b]indistinguishable with $B_2(TO_3)$
[c]indistinguishable with $A_1(TO_1)$

based on comparison with end members. Here, we report temperature-dependent dielectric response in bulk ceramic $KNbO_3$ and KBNNO. Using rigorous lineshape and peak fitting analyses, we show temperature-dependent evolution of the structural and ferroelectric phases in bulk ceramic KBNNO from 100-1000 $cm^{-1}$ for 83 K $< T <$ 873 K, comparing our results with bulk ceramic $KNbO_3$. Finally, we present the results of density functional theoretical analysis, calculating the structural relaxation and electric polarization, and theoretically estimating the $T_c$ in order to compare with our experimental data.

## II. EXPERIMENTAL METHODS

Samples of $[KNbO_3]_{1-x}[BaNi_{1/2}Nb_{1/2}O_{3-\delta}]_x$ ($x = 0$ and 0.1) are synthesized by standard solid-state reaction followed by a sintering process. High purity powders, including $K_2CO_3$ (J.T. Baker, 99.9%), $BaCO_3$ (Cerac, 99.9%), $Nb_2O_5$ (Cerac, 99.95%), and NiO (Cerac, 99%) are dried at appropriate temperatures to remove absorbed moisture. Stoichiometric amounts of starting powders are mixed by ball milling for $\geqslant$ 2 h in ethanol with yttrium-stabilized $ZrO_2$ grinding media. After evaporation of ethanol, the raw mixtures for samples with $x = 0.1$ are calcined at 1073 K for 6 h in a muffle furnace while, for $x = 0$ samples, 873 K for 6 h is used. The calcined powders are ball milled for 12 h to minimize the particle size and then uniaxially pressed into pellets of 8-mm diameter and 2- to 4-mm thickness. In order to minimize the volatilization of K during sintering, all pellet samples are buried in calcined powders with the same composition and encapsulated with platinum foil. Pellets are sintered at temperatures which depend on compositions, with a dwell time of 1 h and 5 K/min ramp rate. KNO pellets are sintered at 1253 K and $x = 0.1$ is sintered at 1418 K. The bulk densities of sintered pellets are calculated through the weights and dimensions of the samples; both the $x = 0$ and 0.1 samples show above 92% relative density.

Powder x-ray diffraction measurements of sintered ceramics are carried out on a Rigaku GiegerFlex D/Max-B diffractometer (40 kV, 30 mA). For dielectric property measurements, sample pellets are first rough polished with 400-grit polishing paper to obtain parallel top and bottom surfaces. Electrodes are then applied to the pellet by coating the polished surfaces with silver paint (Heraeus ST1601-14 type). Platinum lead wires are attached to the surfaces using the same silver paint. Paint is dried and sintered at 1023 K for 20 min to provide a dense electrical contact. The dielectric data are collected with a high-precision impedance-capacitance-resistance meter (Hewlett-Packard, model 4284A) and a high-temperature thermal chamber. The ferroelectric transitions in dense $(K_{0.5}Na_{0.5})NbO_3$ are used to precisely calibrate the temperature [47].

Temperature-dependent Raman spectra are collected in the backscattering configuration $z(x,x+y)\bar{z}$ using a single monochromator (XploRA, Horiba Jobin-Yvon, Edison NJ), 4 mW, 532-nm laser excitation, focused through a 10x objective to a spot diameter of $\approx$10 $\mu$m at an intensity of $1.6 \times 10^3$ W/$cm^2$. Light is dispersed using 2400-gr/mm gratings and collected using a thermoelectrically cooled array detector. The spectral resolution of this confocal micro-Raman instrument under these conditions is $\approx$1.2 $cm^{-1}$. The sample temperature is varied from 83 K to 873 K (Linkham THMS 600, instrumental precision $\pm$0.1 K) in increments of 2.5 K (for $KNbO_3$) and 5 K (for KBNNO) at a heating ramp rate of 5 K/min. The sample is also allowed to equilibrate for 1 min between consecutive Raman scans.

We use density functional theory (DFT) calculations to examine the local structure and polarization caused by substitution of 0.1 $Ba(Ni_{1/2}Nb_{1/2})O_{2.75}$ (BNNO) into KNO. To directly and accurately model the low concentration of Ba and Ni dopant atoms, we use a $4 \times 4 \times 2$ 159-atom supercell, with $x = 0.125$ BNNO content. This cell contains 2 Ni atoms and 4 Ba atoms substituting at 2 Nb and 4 K sites. To maintain charge balance, one O atom is removed, in two different configurations. For the first configuration, the O vacancy is

TABLE II. Summary of optical modes associated with the four structural phases in KNO and KBNNO.

| Phase | Space Group | Point Group | Optical Modes |
|---|---|---|---|
| Rhombohedral | $R3m$ | $C_{3v}^5$ | $3\ A_1(T_z,\alpha_{xx}+\alpha_{yy},\alpha_{zz})\ A_2$[a] $+ 4\ E\ (T_x,T_y,\alpha_{xx}-\alpha_{yy},\alpha_{xy},\alpha_{xz},\alpha_{yz})$ |
| Orthorhombic | $Amm2$ | $C_{4v}^{14}$ | $4\ A_1(T_z,\alpha_{xx},\alpha_{yy},\alpha_{zz}) + A_2(\alpha_{xy}) + 4\ B_1(T_x,\alpha_{xz}) + 3\ B_2(T_y,\alpha_{yz})$ |
| Tetragonal | $P4mm$ | $C_{4v}^1$ | $3\ A_1\ (T_z, \alpha_{xx}+\alpha_{yy},\alpha_{zz}) + B_1(\alpha_{xx}-\alpha_{yy}) + 4\ E(T_x,T_y,\alpha_{xz},\alpha_{yz})$ |
| Cubic | $Pm3m$ | $O_h^1$ | $3\ F_{1u}$[a]$(T_x, T_y, T_z) + F_{2u}$[a] |

[a]mode is not Raman active

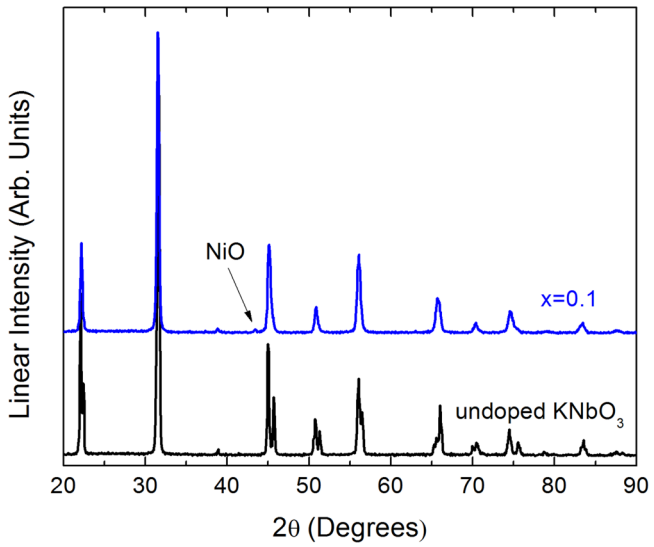


FIG. 1. X-ray diffraction spectra of end member KNO and $x = 0.1$ KBNNO stoichiometry. Arrows indicate the inclusion of NiO. Additional stoichiometries available in Ref. [47].

placed between two Ni atoms located at nearest-neighbor $B$-sites along the $z$ direction while, for the second, the vacancy is located between an Nb and an Ni, and the two Ni are separated by 7 Å. For computational efficiency, we performed all calculations at the $KNbO_3$ lattice constants. This choice is supported by the results of the XRD measurements that show that the lattice parameters of $KNbO_3$ and $x = 0.1$ KBNNO are essentially the same. The positions of the ions were fully relaxed at the DFT + $U$ level of calculations, using Hubbard $U$ values of 3.97 eV and 9.9 eV for Nb and Ni, respectively, as in previous KBNNO calculations [10]. Calculations with other values of $U$ showed only slight dependence of the relaxed structure on the $U$ value, supporting the reliability of our choice of $U$.

The relaxed structures are analyzed for cation displacements, which can then be used to evaluate the effect of the $Ba(Ni,Nb)O_{2.75}$ substitution on the local structure and to estimate the polarization by multiplying the cation displacements by their respective Born effective charge ($Z^*$) values. We also used Berry phase calculations to rigorously evaluate the polarization, with good agreement obtained between the approximate displacement-based and the Berry phase polarization values. The decomposition of $P$ into the contributions of individual cation sites enables analysis of trends in overall $P$ in terms of local structure changes.

## III. RESULTS AND DISCUSSION

The powder x-ray diffraction results show the formation of a stable perovskite for all compositions, while very small NiO impurity peaks are present in samples of $x = 0.1$ (Fig. 1). Dielectric permittivities and losses are obtained as a function of temperature and frequency (Fig. 2). Samples of composition $x = 0.1$ show dielectric anomalies, which indicate phase transitions at 683 K and 533 K. The lack of frequency dependence indicates normal ferroelectric behavior,

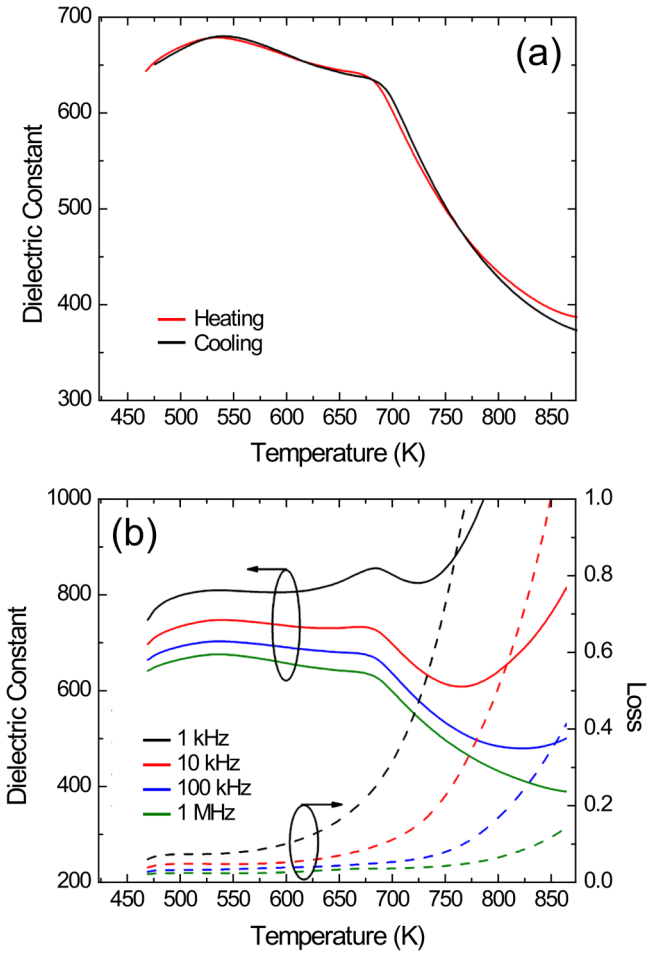


FIG. 2. Temperature dependence of dielectric permittivity measured at 1 MHz for (a) KBNNO $x = 0.1$; heating cycle and cooling cycle are red and black respectively. (b) Temperature-dependent dielectric permittivity and loss of KBNNO $x = 0.1$ for various $E$-field frequencies.

since frequency-dependent dielectric response is characteristic of a relaxor.

Since phonon linewidths are temperature dependent, vibrational mode assignment is most straightforward in low-temperature spectra (Fig. 3, rhombohedral phase). Neither the KNO nor KBNNO samples are single crystalline, and, therefore, the signal measured is an average of many oblique angles not strictly associated with phonon wave vectors either parallel or perpendicular to the specific crystallographic axes that would allow for the proper assignment of transverse and longitudinal optical (TO, LO) phonon modes [48]. Due to this formalism, the modes will be referred to as ≈190 $cm^{-1}$, ≈290 $cm^{-1}$, ≈430 $cm^{-1}$, ≈529 $cm^{-1}$, ≈600 $cm^{-1}$, and ≈836 $cm^{-1}$; respectively, for both KNO and KBNNO polycrystalline samples with the primarily contributing modes denoted in Fig. 3. For simplicity, a single assignment will follow each mode through softening, stiffening, and any abrupt changes due to structural changes in the sample, with the understanding that there are often many modes with overlapping phonon frequency making up a spectral feature. Comparable peak energies are observed in the KBNNO

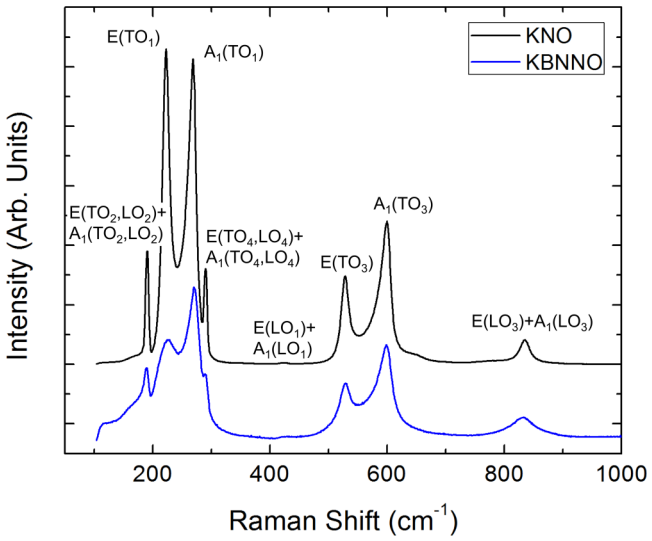


FIG. 3. Raman spectra of the KNO and KBNNO samples in the rhombohedral phase collected at 83 K with approximate mode assignments from bulk and polycrystalline litterature showing overall agreement between end member KNO and solid-solution KBNNO [36,37,49–52].

sample and correspond well to reported mode assignments in $KNbO_3$ [36,37,49–52]. The $TO_1$ mode, associated primarily with ferroelectricity and the polarization of the material, corresponds to the central *B*-site Nb atoms oscillating against the oxygen octahedra and is shown in Fig. 4. This mode is particularly indicative of polarization in the material due to the parallel alignment of the polarization vector and the Nb-O bond. The $TO_2$ mode corresponds to the *A*-site K atoms vibrating counter to the greater $NbO_6$ octahedral structure. The $TO_3$ mode corresponds to the *B*-site Nb atoms and the apical oxygen atoms moving parallel along the polarization vector, antiparallel to the equatorial oxygen atoms. The *A*-site

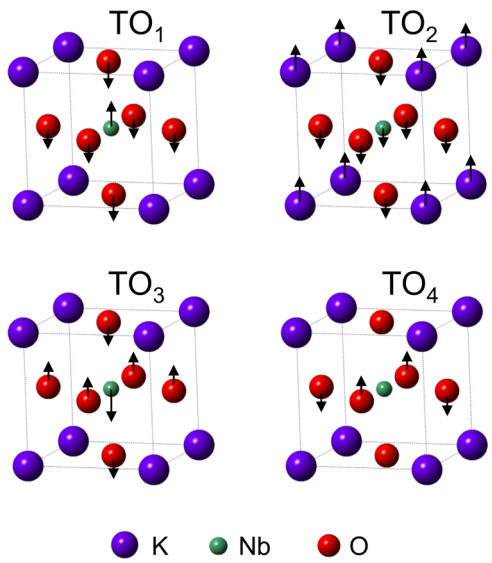


FIG. 4. Ionic displacements associated with the four transverse optical phonons from lattice dynamics calculations [37].

K atoms do not dynamically participate in the $TO_3$ mode. The $TO_4$ mode corresponds to stationary *A*- and *B*-site atoms and apical O atoms, while the equatorial oxygen atoms vibrate out of phase along the polarization direction, with each equatorial oxygen atom moving antiparallel to its nearest equatorial oxygen neighbors.

Temperature-dependent Raman spectra for $KNbO_3$ (KNO) and KBNNO are shown in Fig. 5. Peak fitting analysis is performed to quantify the variation of each peak's intensity, width, and position with temperature [47]. Bose-Einstein correction has been performed before any data analysis of structural phase transitions; in addition, the contour plots and stacked plots are normalized for the convenience of the reader, as the low-temperature data has much greater signal and lower background than the high-temperature data. Transition temperatures are then extracted from the KNO and KBNNO samples based on reported mode assignments, as cited above.

Changes in Raman peak positions and intensities are seen at particular temperatures corresponding to first-order structural phase transitions: rhombohedral (R) → orthorhombic (O) → tetragonal (T) → cubic (C) (Fig. 5). While determination of phase transition temperatures can be done by inspection for some modes, detailed analysis is required for others [47]. For example, the transition temperatures are clear in KNO modes of $\approx$190 $cm^{-1}$, $\approx$290 $cm^{-1}$, $\approx$529 $cm^{-1}$, and $\approx$600 $cm^{-1}$; Fig. 5). By contrast, the peaks in the KBNNO solid solution sample are much broader, and specific modes (e.g., for $\approx$190 $cm^{-1}$ and $\approx$836 $cm^{-1}$), which disappear in the end member upon reaching the cubic phase, do not disappear at temperatures well above the expected transition temperature for the cubic phase in the solid solution. Although the temperature dependence of the relative intensities, peak widths, and position are not as distinct as in KNO, the end member's behaviors can be used as a reference for mode assignment and to extract the phase transition temperatures for KBNNO.

The R → O transition temperature for KNO was established using the relative intensity, mode linewidth, and frequency for the $\approx$190 $cm^{-1}$, $\approx$290 $cm^{-1}$, $\approx$430 $cm^{-1}$, $\approx$529 $cm^{-1}$, and $\approx$600 $cm^{-1}$ modes [47], yielding an R → O transition temperature $T_{R\rightarrow O,\,KNO}$ of 272.0 ± 0.1 K (Table III). For the KBNNO sample the $\approx$190 $cm^{-1}$, $\approx$290 $cm^{-1}$, and $\approx$430 $cm^{-1}$ modes also exhibited abrupt changes, yielding $T_{R\rightarrow O,\,KBNNO} \approx$ 275 ± 8 K. A particularly clear example is seen in Fig. 6(a) where the degenerate $\approx$290 $cm^{-1}$ modes' frequency undergoes a sharp discontinuity which can be clearly observed in the KNO sample. This combination of modes contributing to the peak at $\approx$290 $cm^{-1}$ softens with higher temperatures. The frequency behavior of the $\approx$290 $cm^{-1}$ modes in KBNNO exhibits a transition and softens, although the mode is much more difficult to resolve due to the various neighboring overlapping modes at those temperatures. While the initial frequency discontinuity in the KBNNO sample is more subtle, the softening with temperature is much more dramatic for the solid solution when compared to the end member.

The O → T transition temperature in KNO (512 ± 1 K) is determined from the behavior of the $\approx$190 $cm^{-1}$, $\approx$290 $cm^{-1}$, $\approx$430 $cm^{-1}$, $\approx$529 $cm^{-1}$, and $\approx$600 $cm^{-1}$ modes. The KBNNO transition is ascertained from the $\approx$430 $cm^{-1}$, $\approx$529 $cm^{-1}$ and $\approx$600 $cm^{-1}$ modes with $T_{O\rightarrow T,\,KBNNO}$ of 523 ± 6 K. Determination of this transition temperature in

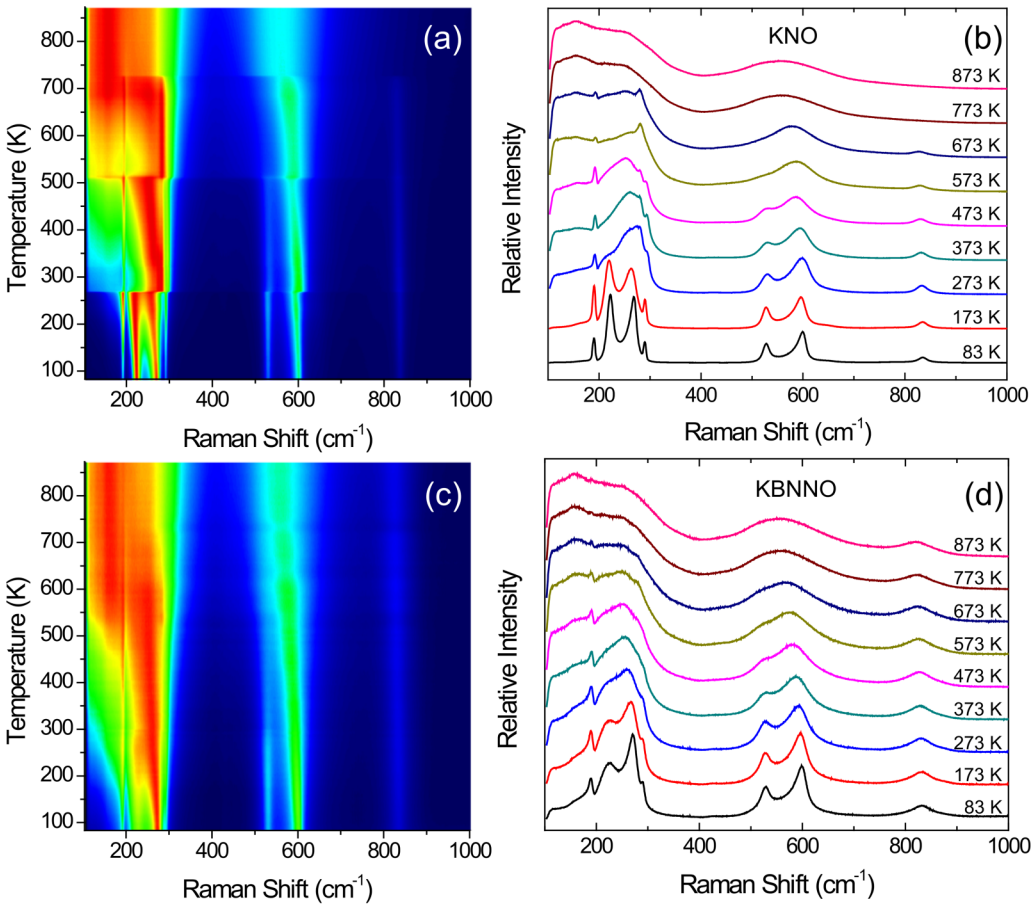


FIG. 5. Raman scattering spectra of KNO ceramic materials as a color map (a) and at selected temperatures (b). Raman spectra of KBNNO ceramic materials is shown as a color map (c) and at selected temperatures (d). Phase transitions more evident in KNO, but both ceramics show spectral characteristics revealing $R \rightarrow O \rightarrow T \rightarrow$ C phase transitions.

KBNNO based on other modes, such as the combination of vibrational modes at ≈290 cm$^{-1}$, could not be accomplished without unacceptably large error. Weighted error analysis is performed using standard expressions for the probability distribution and weighting factors [47]. This effectively removes the contributions of the ≈290 cm$^{-1}$ modes by weighting them by the inverse of their variance such that they do not significantly affect the KBNNO transition temperature. Specifically, the ≈430 cm$^{-1}$ modes are useful for both the KNO and KBNNO samples and are significant for determining the O → T transition [Fig. 6(b)].

Changes in the mode frequency for ≈430 cm$^{-1}$ phonons signal the onset of the orthorhombic phase at ≈273 K. For increasing temperature, the modes at ≈430 cm$^{-1}$ stiffen until the O → T transition occurs, beyond which the modes soften slightly until the frequency stabilizes. A decrease in intensity to the background-noise level prevents analysis at higher temperature. This stiffening and softening behavior around the O → T transition in KNO is used to discern the KBNNO transition temperature by identifying the same stiffening and softening in the much broader behavior of the ≈430 cm$^{-1}$ modes. Without the context provided by the response of KNO, assigning the maximum frequency of these modes is, at best, challenging, considering the various features that affect the relative intensities, linewidths, and frequencies of the Raman modes with temperature, including through structural phase transitions [53–56].

The highest-temperature tetragonal to cubic transition, corresponding to the ferroelectric to paraelectric transition, in the KNO sample occurs at 729.2 ± 0.2 K, as is most easily seen in the ≈190 cm$^{-1}$, ≈529 cm$^{-1}$, ≈600 cm$^{-1}$, and ≈836 cm$^{-1}$ modes. At this temperature, the ≈290 cm$^{-1}$ modes have broadened to the point where the $TO_1$ and $TO_4 + LO_4$ contributions are indistinguishable. Additionally, the modes

TABLE III. Summary of structural phase transition temperatures as determined from Raman.

| | Rhombohedral → Orthorhombic (R → O) | Orthorhombic → Tetragonal (O → T) | Tetragonal → Cubic (T → C) |
|---|---|---|---|
| KNO | 272.0 ± 0.1 K | 512 ± 1 K | 729.2 ± 0.2 K |
| KBNNO | 275 ± 8 K | 523 ± 6 K | 736 ± 7 K |

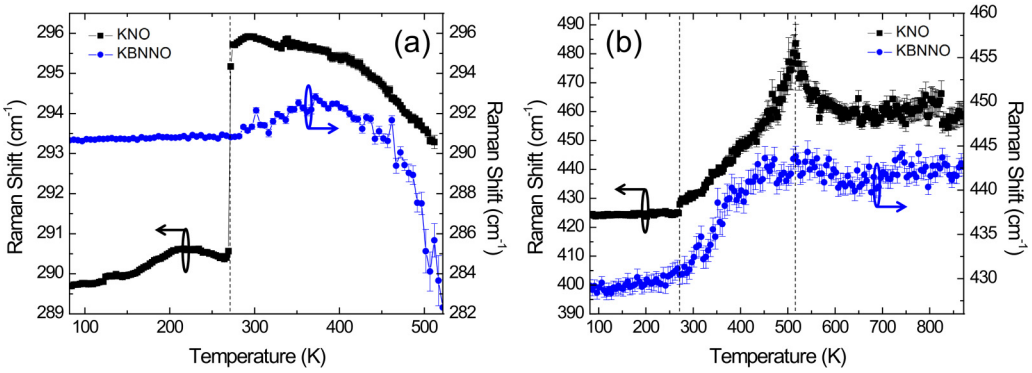


FIG. 6. (a) Temperature dependence of the overlapping phonon modes near 290 $cm^{-1}$. While a >4 $cm^{-1}$ increase in peak energy is seen for KNO, signaling the R → O transition, a much smaller change is observed for KBNNO, as confirmed by analysis of the ≈430 $cm^{-1}$ mode. (b) Temperature dependence of the ≈430 $cm^{-1}$ modes shows a maximum stiffening which signals the O → T phase transition in KNO; a broader, weaker maximum is also seen at the same temperature in KBNNO. Vertical dashed lines correspond to determined phase transition temperatures in KNO.

at ≈290 $cm^{-1}$ and ≈430 $cm^{-1}$ that give signal above the background at lower temperatures have decreased or vanished as expected from previous studies of the mode evolution in KNO [36,37,49–52]. The ≈190 $cm^{-1}$, ≈529 $cm^{-1}$, and ≈600 $cm^{-1}$ modes in the Raman spectra for the KBNNO sample yield $T_{T\rightarrow C,\,KBNNO} \approx 736 \pm 7$ K. Through this transition temperature, the ≈600 $cm^{-1}$ mode condenses into the ≈529 $cm^{-1}$ mode to become a single mode at high temperatures [38] for both KNO and KBNNO (Fig. 5). The temperature dependence of the Raman mode frequency for the ≈529 $cm^{-1}$ mode can be traced until it becomes indistinguishable with the ≈600 $cm^{-1}$ mode [Fig. 7(a)]. As expected with ≈529 $cm^{-1}$, there is a general softening through the rhombohedral, orthorhombic, and tetragonal phases and transitions, and significant changes to the mode linewidth through the various transitions as well [Fig. 7(b)]. Coalescing of ≈529 $cm^{-1}$ and ≈600 $cm^{-1}$ to degeneracy near ≈560 $cm^{-1}$ is most clearly seen in [Fig. 7(c)]. The amplitude of ≈600 $cm^{-1}$ in KNO is seen to increase discontinuously at the transition temperature we assign to the merging of this mode with the ≈529 $cm^{-1}$. This justifies allowing the fitted amplitude of ≈600 $cm^{-1}$ to decrease to zero as the two modes become degenerate [47,53,55].

DFT calculations are performed for cation configurations where the vacancy is located between two Ni atoms and also where the vacancy is located between Ni and Nb atoms, with another Ni surrounded by six O atoms. We find that the configuration with the vacancy between the two Ni is lower in energy by 1.48 eV. Such a large energy difference suggests that KBNNO will mostly contain Ni-$O_{vac}$-Ni configurations.

In a $4 \times 4 \times 2$ supercell, $x$ and $y$ are the long directions and $z$ is the short direction. We place the two Ni along the $x$ direction and relax all ions starting with the cations displaced along ⟨111⟩. Berry phase polarization calculations for the relaxed structure indicate that the values of the polarization components in the $x$, $y$, and $z$ directions are 0.142 $C/m^2$, 0.192 and 0.208 $C/m^2$, respectively. The polarization values in the $y$ and $z$ directions are slightly smaller than the 0.233 $C/m^2$ obtained for the $x$, $y$, and $z$ $P$ components of the $KNbO_3$ parent material in the 0 K rhombohedral phase. The polarization component along the $x$ direction is more significantly reduced to 0.142 $C/m^2$. Examination of the local displacements shows that the introduction of BNNO leads to a distribution of the local Nb displacements, with Nb off-centering magnitudes in a given Cartesian direction varying from 0 to 0.135 Å with the average Nb displacement magnitude of 0.16 Å. These average displacement values are smaller than the 0.103 Å displacements along the $x$, $y$, and $z$ direction found for $KNbO_3$ by our DFT calculations.

Using a previously established correlation between the experimentally observed $T_c$ and the square of the 0 K DFT polarization [57–61], we estimate a decreased $T_c$ for KBNNO of either ≈433 K based on the average total $P$, or ≈573 K based on the average magnitude of the Nb displacements related to the local polarization. While also predicting a stable room-temperature ferroelectricity in KBNNO, these values underestimate both the dielectric tetragonal to cubic (T-C) transition temperature of 683 K as well as the 736 K T-C transition temperature extracted from the Raman results. This discrepancy could be ascribed to the somewhat qualitative nature of the correlation between $T_c$ and $P^2$ for materials with different local structures. The presence of Ni + $O_{vac}$ introduces structural motifs into KBNNO that are entirely absent in KNO, diminishing the predictive accuracy of the $T_c - P^2$ correlation.

The DFT finding of a distribution of Nb displacement magnitudes and variation in the local structure is consistent with broadening in both the dielectric and Raman data, including the Raman linewidth. In particular, the temperature evolution of the Raman shift used to assign the T-C transition temperature changes from an abrupt drop at $T_c$ observed for KNO to a gradual decrease to a constant value observed for KBNNO. It is likely that the distribution of local environments found in KBNNO leads to a broader distribution of Raman shifts, with the local environments displaying enhanced (relative to KNO) Nb displacements accounting for the higher temperature plateauing of the Raman shift that signifies the presence of the T-C transition. Such dependence of the Raman shift on the distribution of local structures (i.e., on the strong displacement contributions) is perhaps the explanation for the disagreement between the enhanced $T_c$ found by Raman results and the decreased $T_c$ found by the dielectric measurements. The dielectric results are given by the average structure of

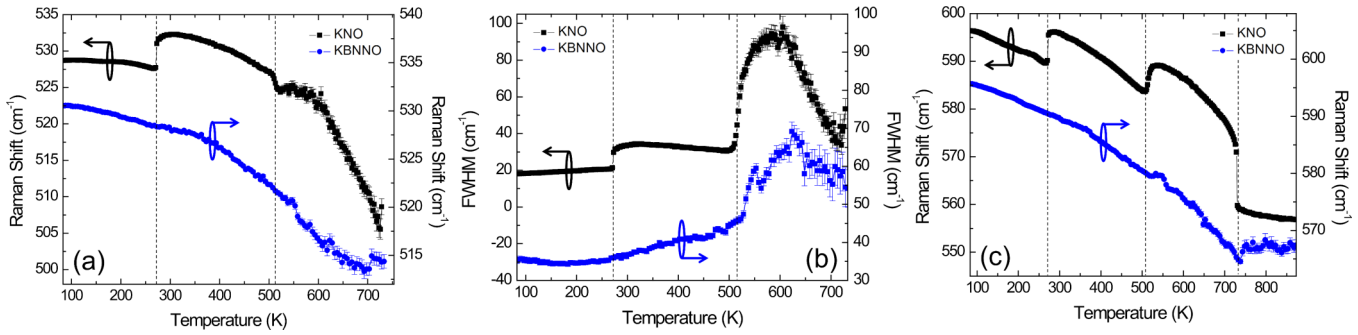


FIG. 7. Comparison of the fitted temperature dependencies of the ≈529 cm$^{-1}$ and ≈600 cm$^{-1}$ modes (a) energy and (b) linewidth in KNO and KBNNO, enabling extraction of the O → T transition temperature; the ≈529 cm$^{-1}$ modes become degenerate with the ≈600 cm$^{-1}$ in the cubic phase and is only shown in (c). (c) Comparison of the ≈600 cm$^{-1}$ mode softening in KNO and KBNNO. The behavior of the KNO and KBNNO modes here is qualitatively similar and, upon phase transition, the ≈600 cm$^{-1}$ becomes degenerate with the ≈529 cm$^{-1}$ modes to collect around 560 cm$^{-1}$ enabling determination of T → C transition temperatures.

the material, where a decrease in the displacement and $P$ is observed for KBNNO, corresponding to a less stable $P$ and a lower FE-PE transition temperature. On the other hand, the Raman measurements are sensitive to the variation in the local structure, where some local environments exhibit enhanced 0 K displacements that are likely to persist to higher temperature than the FE structure in the parent KNO material.

## IV. CONCLUSIONS

Dielectric permittivity measurements and Raman spectroscopy are used to probe temperature-dependent structural and ferroelectric phase evolution. Changes in the temperature-dependent Raman shifts are diffused in KBNNO as compared with abrupt transitions observed in the end member KNO. Taken together with variations in DFT-calculated local atom displacements and local and averaged polarizations (the extent of applicability of $T_c - P^2$ scaling notwithstanding), and the absence of frequency dispersion in the dielectric permittivity, these results indicate persistence of ferroelectric ordering in KBNNO to temperatures that approach the $T_c$ of the end member $KNbO_3$. This identification of structural and ferroelectric phases, combined with the ability to tune these solid-solution ceramic materials compositionally, highlights these oxides' promising application as semiconducting ferroelectric absorbers and carrier-separating layers in novel photovoltaic devices.

## ACKNOWLEDGMENTS

Work at Drexel supported by the US Army Research Office under Grant No. W911NF-14-1-0500. G.X. was supported by the National Science Foundation under Grant No. DMR 1608887 and J.E.S. also acknowledges support from Grant No. DMR 1124696. A.M.R. was supported by the Department of Energy Office of Basic Energy Sciences, under Grant No. DE-FG02-07ER46431. The authors acknowledge the use of the Core Facilities at Drexel University and Raman instrumentation acquisition via the ARO Defense University Research Instrumentation Program. The authors acknowledge computational support from the National Energy Research Scientific Computing Center of the Department of Energy.

[1] S. Y. Yang, J. Seidel, S. J. Byrnes, P. Shafer, C. H. Yang, M. D. Rossell, P. Yu, Y. H. Chu, J. F. Scott, J. W. Ager, L. W. Martin, and R. Ramesh, Nat. Nanotechnol. **5**, 143 (2010).

[2] J. Seidel, D. Fu, S.-Y. Yang, E. Alarcón-Lladó, J. Wu, R. Ramesh, and J. W. Ager, Phys. Rev. Lett. **107**, 126805 (2011).

[3] M. Alexe and D. Hesse, Nat. Commun. **2**, 256 (2011).

[4] R. Nechache, C. Harnagea, S. Licoccia, E. Traversa, A. Ruediger, A. Pignolet, and F. Rosei, Appl. Phys. Lett. **98**, 202902 (2011).

[5] S. M. Young and A. M. Rappe, Phys. Rev. Lett. **109**, 116601 (2012).

[6] S. M. Young, F. Zheng, and A. M. Rappe, Phys. Rev. Lett. **109**, 236601 (2012).

[7] J. Kreisel, M. Alexe, and P. A. Thomas, Nat. Mater. **11**, 260 (2012).

[8] D. Daranciang, M. J. Highland, H. Wen, S. M. Young, N. C. Brandt, H. Y. Hwang, M. Vattilana, M. Nicoul, F. Quirin, J. Goodfellow, T. Qi, I. Grinberg, D. M. Fritz, M. Cammarata, D. Zhu, H. T. Lemke, D. A. Walko, E. M. Dufresne, Y. Li, J. Larsson, D. A. Reis, K. Sokolowski-Tinten, K. A. Nelson, A. M. Rappe, P. H. Fuoss, G. B. Stephenson, and A. M. Lindenberg, Phys. Rev. Lett. **108**, 087601 (2012).

[9] B. Yang, Y. Yuan, P. Sharma, S. Poddar, R. Korlacki, S. Ducharme, A. Gruverman, R. Saraf, and J. Huang, Adv. Mater. **24**, 1455 (2012).

[10] I. Grinberg, D. V. West, M. Torres, G. Gou, D. M. Stein, L. Wu, G. Chen, E. M. Gallo, A. R. Akbashev, P. K. Davies, J. E. Spanier, and A. M. Rappe, Nature **503**, 509 (2013).

[11] V. Fridkin, IEEE Trans. Sonics Ultrason. **60**, 1551 (2013).

[12] A. Bhatnagar, A. R. Chaudhuri, Y. H. Kim, D. Hesse, and M. Alexe, Nat. Commun. **4**, 2835 (2013).

[13] Z. Xiao, Q. Dong, P. Sharma, Y. Yuan, B. Mao, W. Tian, A. Gruverman, and J. Huang, Adv. Energy Mater. **3**, 1672 (2013).

[14] R. Nechache, C. Harnagea, S. Li, L. Cardenas, W. Huang, J. Chakrabartty, and F. Rosei, Nat. Photon. **9**, 61 (2015).

[15] A. Zenkevich, Y. Matveyev, K. Maksimova, R. Gaynutdinov, A. Tolstikhina, and V. Fridkin, Phys. Rev. B **90**, 161409 (2014).

[16] Y. Yuan, Z. Xiao, B. Yang, and J. Huang, J. Mater. Chem. A **2**, 6027 (2014).

[17] J. P. Chakrabartty, R. Nechache, C. Harnagea, and F. Rosei, Opt. Express **22**, A80 (2014).

[18] J. E. Spanier, V. M. Fridkin, A. M. Rappe, A. R. Akbashev, A. Polemi, Y. Qi, Z. Gu, S. M. Young, C. J. Hawley, D. Imbrenda, G. Xiao, A. L. Bennett-Jackson, and C. L. Johnson, Nat. Photon. **10**, 611 (2016).

[19] A. A. Grekov, M. A. Malitskaya, V. D. Spitsina, and V. M. Fridkin, Kristallografiya **15**, 500 (1970).

[20] A. M. Glass, D. von der Linde, and T. J. Negran, Appl. Phys. Lett. **25**, 233 (1974).

[21] V. Belincher and B. Sturman, Phys. Usp. **23**, 199 (1980).

[22] B. Sturman and V. Fridkin, *The Photovoltaic and Photorefractive Effects in Noncentrosymmetric Materials* (Gordon and Breach, Philadelphia, 1992).

[23] J. W. Bennett, I. Grinberg, and A. M. Rappe, J. Am. Chem. Soc. **130**, 17409 (2008).

[24] G. Y. Gou, J. W. Bennett, H. Takenaka, and A. M. Rappe, Phys. Rev. B **83**, 205115 (2011).

[25] T. Qi, I. Grinberg, and A. M. Rappe, Phys. Rev. B **83**, 224108 (2011).

[26] F. Wang, I. Grinberg, L. Jiang, S. M. Young, P. K. Davies, and A. M. Rappe, Ferroelectrics **483**, 1 (2015).

[27] F. Wang, S. M. Young, F. Zheng, I. Grinberg, and A. M. Rappe, Nat. Commun. **7**, 10419 (2016).

[28] F. Wang and A. M. Rappe, Phys. Rev. B **91**, 165124 (2015).

[29] W. Zhou, H. Deng, P. Yang, and J. Chu, Appl. Phys. Lett. **105**, 111904 (2014).

[30] G. H. Haertling and C. E. Land, J. Am. Ceram. Soc. **54**, 1 (1971).

[31] L. Davis and L. G. Rubin, J. Appl. Phys. **24**, 1194 (1953).

[32] B. T. Matthias and J. P. Remeika, Phys. Rev. **82**, 727 (1951).

[33] G. Shirane, R. Newnham, and R. Pepinsky, Phys. Rev. **96**, 581 (1954).

[34] M. Fontana and C. Razzetti, Solid State Commun. **17**, 377 (1975).

[35] J. Hurrell and D. Bozinis, Solid State Commun. **17**, 1541 (1975).

[36] M. D. Fontana, G. Dolling, G. E. Kugel, and C. Carabatos, Phys. Rev. B **20**, 3850 (1979).

[37] M. D. Fontana, G. E. Kugel, G. Metrat, and C. Carabatos, Phys. Status Solidi B **103**, 211 (1981).

[38] M. D. Fontana, G. Metrat, J. L. Servoin, and F. Gervais, J. Phys. C **17**, 483 (1984).

[39] M. D. Fontana, A. Ridah, G. E. Kugel, and C. Carabatos-Nedelec, J. Phys. C **21**, 5853 (1988).

[40] R. Currat, H. Buhay, C. H. Perry, and A. M. Quittet, Phys. Rev. B **40**, 10741 (1989).

[41] E. Buixaderas, D. Nuzhnyy, I. Gregora, S. Kamba, M. Berta, B. Malic, and M. Kosec, IEEE Trans. Sonics Ultrason. **56**, 1843 (2009).

[42] N. Klein, E. Hollenstein, D. Damjanovic, H. J. Trodahl, N. Setter, and M. Kuball, J. Appl. Phys. **102**, 014112 (2007).

[43] A. Bartasyte, J. Kreisel, W. Peng, and M. Guilloux-Viry, Appl. Phys. Lett. **96**, 262903 (2010).

[44] L. Luisman, A. Feteira, and K. Reichmann, Appl. Phys. Lett. **99**, 192901 (2011).

[45] H. J. Trodahl, N. Klein, D. Damjanovic, N. Setter, B. Ludbrook, D. Rytz, and M. Kuball, Appl. Phys. Lett. **93**, 262901 (2008).

[46] I. S. Golovina, V. P. Bryksa, V. V. Strelchuk, I. N. Geifman, and A. A. Andriiko, J. Appl. Phys. **113**, 144103 (2013).

[47] See Supplemental Material http://link.aps.org/supplemental/10.1103/PhysRevB.96.054117 for description of analysis, additional synthesis details, x-ray diffraction measurements, and additional dielectric constant and loss measurements which includes Refs. [53,55,63–71]

[48] R. Loudon, Adv. Phys. **13**, 423 (1964).

[49] G. E. Kugel, M. D. Fontana, J. Vamvakas, and C. Carabatos, *Raman Spectroscopy, Linear and Nonlinear: Proceedings of the Eighth International Conference on Raman Spectroscopy, Bordeaux, France, 6-11 September* (John Wiley and sons, 1982) p. 457.

[50] A. M. Quittet, J. L. Servoin, and F. Gervais, J. Phys. (France) **42**, 493 (1981).

[51] D. G. Bozinis and J. P. Hurrell, Phys. Rev. B **13**, 3109 (1976).

[52] A. V. Postnikov, T. Neumann, and G. Borstel, Phys. Rev. B **50**, 758 (1994).

[53] A. M. Quittet, M. I. Bell, M. Krauzman, and P. M. Raccah, Phys. Rev. B **14**, 5068 (1976).

[54] L. H. Robins, D. L. Kaiser, L. D. Rotter, P. K. Schenck, G. T. Stauf, and D. Rytz, J. Appl. Phys. **76**, 7487 (1994).

[55] G. E. Kugel, M. D. Fontana, J. Vamvakas, and C. Carabatos, Ferroelectrics **55**, 27 (1984).

[56] M. Fontana, G. Kugel, J. Vamvakas, and C. Carabatos, Solid State Commun. **45**, 873 (1983).

[57] S. C. Abrahams, S. K. Kurtz, and P. B. Jamieson, Phys. Rev. **172**, 551 (1968).

[58] I. Grinberg and A. M. Rappe, Phys. Rev. B **70**, 220101 (2004).

[59] I. Grinberg and A. M. Rappe, Phys. Rev. Lett. **98**, 037603 (2007).

[60] J. Chen, K. Nittalla, J. L. Jones, P. Hu, and X. Xing, Appl. Phys. Lett. **96**, 252908 (2010).

[61] A. Berenov, F. L. Goupil, and N. Alford, Sci. Rep. **6**, 28055 (2016).

[62] A. V. Postnikov and G. Borstel, Phys. Rev. B **50**, 16403 (1994).

[63] *IGOR Pro*, version 6.0 ed. (WaveMetrics, Inc., Lake Oswego, OR, 2008).

[64] W. H. Press, S. A. Teukolsky, W. T. Vetterling, and B. P. Flannery, *Numerical Recipes in C*, 2nd ed., The Art of Scientific Computing (Cambridge University Press, New York, 1992).

[65] A. G. Palmer III, M. Rance, and P. E. Wright, J. Am. Chem. Soc. **113**, 4371 (1991).

[66] D. J. Hudson, J. Am. Stat. Assoc. **61**, 1097 (1966).

[67] A. Ganse, Multi-Phase Linear Regression, Line 96 was edited to correct a sum of residuals squared error, https://github.com/aganse/MultiRegressLines.matlab.

[68] G. Holton, *Value-at-Risk: Theory and Practice* (Academic Press, San Diego, 2003).

[69] P. R. Renne, A. L. Deino, R. C. Walter, B. D. Turrin, C. C. Swisher, III, T. A. Becker, G. H. Curtis, W. D. Sharp, and A.-R. Jaouni, Geology **22**, 783 (1994).

[70] I. Kirsch, B. J. Deacon, T. B. Huedo-Medina, A. Scoboria, T. J. Moore, and B. T. Johnson, PLOS Medicine **5**, e45 (2008).

[71] J.-F. Li, K. Wang, F.-Y. Zhu, L.-Q. Cheng, and F.-Z. Yao, J. Am. Ceram. Soc. **96**, 3677 (2013).